A Study of $NaBi(WO_4)_2$ as a Cherenkov Radiator

David Gordon Williams
New Orleans, Louisiana

B.S., Tulane University, 1991

A Thesis presented to the Graduate Faculty
of the University of Virginia in Candidacy for the Degree of
Master of Science

Department of Physics

University of Virginia
August, 2002

Bradley Cox

Kenneth S. Nelson

20020712 128

Acknowledgements:

As I near the completion of my thesis and current graduate work, I am very mindful that while I am credited for this work, I could not have completed it without help from so many people.

I would like to thank my advisor, Dr. Brad Cox, and my first reader, Dr. Ken Nelson, for their guidance and direction throughout my entire studies. The wonderful blend of their techniques and talents truly helped me to learn and develop.

I must give special thanks to the entire group at the High Energy Lab for not only their knowledge, but also their companionship. I would like to specifically recognize Dr. Alexander Ledovskoy, Mike Arenton, Alexander Golossanov, Mike Ronquest, John Shields, and Diana Stokely. You have all made a personal impact on my work and me. Thanks to all of my classmates, who made the hard times barable and the good times better.

Many thanks go to Dr. Ed Dukes for allowing me to use his photon tracing program, which formed the basis for my simulations. I must thank Dr. David Metcalf, who treated me as one of his own students, of the Chemistry Department for the use of the Cary Spectrophotometer. I would also like to thank Dr. David Mzhavia from Dubna Institute, Russia for providing the samples of $NaBi(WO_4)_2$ in order for us to conduct these studies.

Contents

List of Figures

List of Tables

1   Introduction

Purpose: The purpose of this thesis is to examine the properties of $NaBi(WO_4)_2$ and determine its usefulness as a Cherenkov radiator. An implicit requirement in this process is to determine the best configuration of a counter using $NaBi(WO_4)_2$ to detect the Cherenkov photons using a photomultiplier tube.

1.1   Motivation for Studying $NaBi(WO_4)_2$

The motivation for studying $NaBi(WO_4)_2$ was to determine its effectiveness as an electromagnetic calorimeter for the proposed experiment at Fermi National Accelerator Laboratory (FNAL), Kaons At the Main Injector (KAMI) [1]. A calorimeter is a device used to measure the energy and position of incident particles, since the energy deposited in the calorimeter is proportional to the path length of the particles in the shower produced by the incident particle. This energy is usually measured in one of two ways, scintillation radiation or Cherenkov radiation, depending on the properties of the material. Scintillation radiation is produced by the ionization of atoms in the detector and involves a time constant for the material since the optical photons emitted after the excited electron relaxes are what is measured to determine the energy deposited. Cherenkov radiation, described in detail in section 1.2, is prompt and does not have an associated time constant. This is an advantage of Cherenkov detectors, especially when there is a high flux of incident particles. KAMI intended to use $NaBi(WO_4)_2$ as the Cherenkov detector in an attempt to identify photons and neutrons near or in the region of the beam. Since the $NaBi(WO_4)_2$ was to be positioned in the neutral

beam, the radiation hardness of the Cherenkov detector was a primary concern. $NaBi(WO_4)_2$ has a radiation hardness of up to 10^7 rad [2] and thus was an excellent candidate material for the job. Additionally $NaBi(WO_4)_2$ is planned to be used in the E391A experiment to be conducted at KEK in Japan [3].

1.2   Cherenkov Radiation / Cherenkov Detectors

Cherenkov radiation is one of the many ways in which a charged particle causes the emission of radiation when passing through a medium. It was first observed by Cherenkov in 1934 and the first published explanation of the radiation was in 1937 (the Frank–Tamm result) [4]. While most types of radiation come from either scattering or acceleration of the charged particle, Cherenkov radiation results from an electromagnetic wave created by a charged particle traveling at velocities above the velocity of light in the medium inducing electric dipoles within the medium. The photons comprising this wave are emitted in the shape of a cone. The cone of radiation is the only radiation that constructively interferes and is able to propagate any significant distance from the path of the charged particle. The emission angle of the photons, also known as the Cherenkov angle (θ_c), is similar to the shock wavefront of supersonic flight.

A more quantitative description of Cherenkov radiation is based in the fact that it is radiation emitted by a charged particle that is traveling faster than the speed of light in a medium. First look at the electromagnetic fields at a point, due to a charged particle moving relativistically in the x direction. Figure 1 shows a charged particle (frame K') moving with velocity, v, and distance of closest approach, b, to the observation point (frame K). Since the charged particle is as-
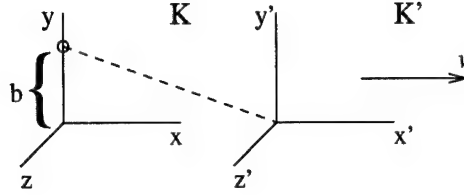
Figure 1: Diagram depicting a charged particle moving with relativistic velocity, v, and impact parameter, b.

sumed to be moving only in the x direction, only the E_1, E_2, and B_3 components are non-zero [4].

$$E_1(\omega) = -\frac{iZe\omega}{v^2}\sqrt{2/\pi}\left[\frac{1}{\epsilon(\omega)} - \beta^2\right]K_0(\lambda b) \qquad (1)$$

$$E_2(\omega) = \frac{Ze}{v}\sqrt{2/\pi}\frac{\lambda}{\epsilon(\omega)}K_1(\lambda b) \qquad (2)$$

$$B_3(\omega) = \beta\,\epsilon(\omega)\,E_2(\omega) \qquad (3)$$

In the above equations, Z represents the charge of the particle, e is the charge of the electron, v is the velocity of the particle, ϵ is the permittivity of the medium as a function of frequency, λ is a parameter defined explicitly in equation (9), and lastly K_0 and K_1 are the modified Bessel functions. The starting point in determining the nature of Cherenkov radiation is looking at the amount of energy deposited in a medium per unit length $\left(\frac{dE}{dx}\right)$ by a charged particle as stated in

equation $(4)^1$ below [4].

$$\left(\frac{dE}{dx}\right)_{b>a} = -ca \int_0^\infty B_3^*(\omega)E_1(\omega)d\omega \tag{4}$$

In equation (4), b represents the impact parameter ($\perp$ distance from the particle's trajectory or distance of closest approach), a is the distance to a distent collision (taken to be of atomic dimensions, $10^{-10}\,m$), E_1 the electric field in the x direction, B_3 the magnetic field in the z direction, both E_1 and B_3 are functions of the frequency (ω), and the particle's velocity is solely in the x direction. Since Cherenkov radiation is observable far away from the path of the particle and is not due to energy which is deposited into the material only a short distance from the path of the charged particle, we must examine the asymptotic forms of the electric and magnetic fields (eq 1, 2, 3) in the far region. In the far region, K_0 and K_1 take on their asymptotic forms and in this limit the electric and magnetic fields become [4]:

$$E_1(\omega, b) \rightarrow \frac{iZe\omega}{c^2}\left[1 - \frac{1}{\beta^2\epsilon(\omega)}\right]\frac{e^{-\lambda b}}{\sqrt{\lambda b}} \tag{5}$$

$$E_2(\omega, b) \rightarrow \frac{Ze}{v\,\epsilon(\omega)}\sqrt{\frac{\lambda}{b}}\,e^{-\lambda b} \tag{6}$$

$$B_3(\omega, b) \rightarrow \beta\,\epsilon(\omega)\,E_2(\omega, b) \tag{7}$$

The Cherenkov radiation emitted by a charged particle is plane polarized in the plane formed by the direction of the particle and the direction of the photon. Now in the far region the energy loss per unit length from equation (4) takes the

---

[1]Cherenkov radiation is closely related to the density effect in energy loss, except they are a result of opposite limiting cases. For Cherenkov radiation $|\lambda a| \gg 1$ and for the density effect $|\lambda a| \ll 1$.

form as given below in equation (8).

$$\left(\frac{dE}{dx}\right)_{b>a} \rightarrow -\frac{Z^2 e^2}{c^2} Re \int_0^\infty i\sqrt{\frac{\lambda^*}{\lambda}}\,\omega \left[1 - \frac{1}{\beta^2 \epsilon(\omega)}\right] e^{-(\lambda + \lambda^*)\,a}\,d\omega \qquad (8)$$

Based on this equation, the only way in which energy (radiation) can be non–zero in the far region is for λ to be purely imaginary. If λ has any real part, then the energy goes to zero in the far region, thus no radiation. With λ purely imaginary, the factor $e^{-(\lambda + \lambda^*)a} = 1$. We must examine λ (as given below) to determine the conditions for which it will be imaginary.

$$\lambda = \frac{\omega}{v}\sqrt{1 - \beta^2 \epsilon(\omega)} \qquad (9)$$

So in order for λ to be purely imaginary, $\beta^2 \epsilon(\omega) > 1$ must be satisfied. With this condition and recalling that $v_{part} = \beta c_{vac}$ and $n(\omega) = \sqrt{\epsilon(\omega)} = \sqrt{\frac{\mu\epsilon}{\mu_0\epsilon_0}} = \frac{c_{vac}}{c_{med}}$, it is easy to see that the following condition is also true.

$$v_{part} > \frac{c_{vac}}{\sqrt{\epsilon(\omega)}} \quad or \quad v_{part} > c_{med} \qquad (10)$$

Thus the velocity of the particle in the medium must be greater than the speed of light in the medium in order for λ to be purely imaginary and for Cherenkov radiation to be emitted. Cherenkov radiation is only produced in cases where the charged particle is traveling faster than a given threshold speed which is based on the index of refraction of the medium.

$$\beta_t = 1/n \qquad (11)$$

Since λ is purely imaginary, $\sqrt{\lambda^*/\lambda} = i$ and equation (8) simplifies to equation (12) below. So the expression for the energy radiated as Cherenkov radiation per unit length the particle has traversed takes the form:

$$\left(\frac{dE}{dx}\right)_{ch\,rad} = \frac{(Ze)^2}{c^2} \int_{\epsilon(\omega)>(1/\beta^2)} \omega \left(1 - \frac{1}{\beta^2\epsilon(\omega)}\right) d\omega \qquad (12)$$

While equation (12) determines the energy radiated by the particle, it is typically much more useful to have the expression for the number of photons per unit length as a function of wavelength. In order to get such an expression, first change to a double differential form and change from ω to λ using $\omega = \frac{2\pi c}{\lambda}$ and $d\omega = \frac{2\pi c}{\lambda^2}d\lambda$. This becomes equation (13) below.

$$\left(\frac{d^2E}{dxd\lambda}\right) = \frac{(2\pi Ze)^2}{\lambda^3} \left(1 - \frac{1}{\beta^2\epsilon(\omega)}\right) \qquad (13)$$

From this point making use of the chain rule for differentials $\frac{dE}{dx} = \frac{dEdN}{dNdx}$ and an expression for energy in terms of lambda, $E = \frac{N2\pi\hbar c}{\lambda}$ in differential form $\frac{dE}{dN} = \frac{2\pi\hbar c}{\lambda}$ equation (13) simplifies to become equation (14) as shown below. This equation will be used in the Monte Carlo simulation detailed later in section 3.

$$\left(\frac{d^2N}{dxd\lambda}\right) = \frac{2\pi\alpha Z^2}{\lambda^2} \left(1 - \frac{1}{\beta^2 n^2(\lambda)}\right) \qquad (14)$$

In equation (14), α is the electromagnetic fine structure constant, $\alpha = \frac{e^2}{\hbar c}$ and n is the index of refraction, $n(\lambda) = \sqrt{\epsilon(\lambda)}$.

The two primary characteristics of Cherenkov radiation, the velocity threshold (β_t) and the angle of emission (θ_c), make Cherenkov detectors a popular method

for charged particle identification in the particle physics arena. The detectors come in two basic types: threshold or differential. As the name implies, the threshold detector determines the particle's identity based on the β_t at which Cherenkov radiation begins to be emitted. As was shown in equation (11), β_t depends only on the index of refraction of the medium[2], $\beta_t = 1/n$. So a medium with a higher index of refraction results in a lower β_t. Additionally, the index of refraction for gas detectors can be adjusted by changing the pressure or by changing the gas mixture in the detector. Once the parameters are set, a *yes* or *no* criteria determines the identity of the particle. *Yes,* β is above threshold and Cherenkov radiation is emitted or *no,* β is below threshold and no Cherenkov radiation is emitted.

The differential detector, on the other hand, determines the particle's identity based on the Cherenkov angle θ_c at which the radiation is emitted. θ_c, as of yet undefined, is determined in the following manner. By applying Huygens' Principle to the photons being emitted from the path of the particle, the only radiation that is coherent and observable is that which is emitted at a particular angle. As seen in Figure 2, the angle is dictated by the distance the radiation has traveled $\left(\frac{c_{vac}}{n}\right)t$ in a given time t and the distance the particle has traveled $(\beta c_{vac})t$ in the same time interval [5]. As can be seen from Figure 2, the Cherenkov angle is a function of β and n alone, as shown in the equations below.

$$cos\theta_c = \frac{1}{\beta n} \tag{15}$$

---

[2]Technically the index of refraction is a function of the wavelength of the emitted radiation, but generally it is taken to be constant over a limited range of wavelengths, such as the sensitivity range of the cathode in a photomultiplier tube.
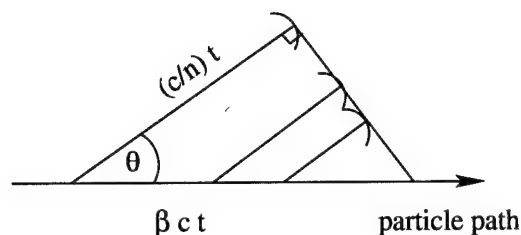
Figure 2: Cherenkov Angle.

$$\theta_c \;=\; cos^{-1}\left(\frac{1}{\beta n}\right) \tag{16}$$

The differential detector is more effective than the threshold detector in cases when there is a mixture of both particle type and momenta. One typical configuration of the differential detector is the Ring Imaging Cherenkov (RICH) detector. The Cherenkov angle is measured by using a spherical or parabolic mirror in order to focus the Cherenkov radiation onto a plane, thus creating a ring around the particle's trajectory. The challenge in this process is to produce enough photons and to conduct effective pattern recognition and to separate the ring under examination from the rings of other particles. Enough photons are needed in order to offset any aberrations (smearing of the ring image) of a geometric or chromatic nature. While many photons may be produced by the charged particle, they must produce photo–electrons in devices such as photomultiplier tubes (PMT) or hybrid photomultiplier devices (HPD) in order to be detected. The number of photo–electrons is smaller then the number of Cherenkov photons by the following factors: the quantum efficiency of the PMT, the transmission coefficient for

radiation reaching the PMT cathode[3], and the efficiency of the detector. Since there will be numerous overlapping rings produced, effective pattern recognition is essential to extract individual rings from the sum of all signals produced in the imaging device whether composed of PMT arrays or HPDs.

For both threshold and RICH Cherenkov detectors, knowing β_t or θ_c alone does not independently identify the particle in question. The particle's momentum must also be known in order to identify the particle type. Once the particle's momentum and β are determined, it is possible to identify the particle by its mass. Since $E = \gamma m c^2$ and $p = \gamma m v$ then $E = \frac{pc}{\beta} = \sqrt{p^2 c^2 + m^2 c^4}$ and from this it is evident how the mass depends on momentum and β as shown in equation (17) below.

$$m = \frac{p}{c}\sqrt{\frac{1}{\beta^2} - 1} \tag{17}$$

Cherenkov radiation and Cherenkov detectors play an important role in particle identification in experimental particle physics. A charged particle's identity can be determined to a high degree of certainty by using a Cherenkov detector, as long as the momentum of the particle is known.

---

[3]The transmission coefficient generally depends on several interfaces of various materials, such as the detector, glass, silicone, or air.

2 Experimental Setup

All of the equipment for the experimental setup was located at the High Energy Physics Laboratory on the campus of the University of Virginia. The coordinates and elevation of this location are 38°02′ N latitude, 78°31′ W longitude, and 710′ above sea level.

2.1 Beam Characteristics

The particles used in all of the Cherenkov radiation studies for this thesis were produced by cosmic ray showers. So a good understanding of the spectrum of cosmic rays at ground level is important to properly understand the collected Cherenkov data. Cosmic rays at ground level are all secondaries that are a result of the primary cosmic ray hitting the upper atmosphere and causing a cascade. While the primaries are mainly electrons, protons, helium, carbon, oxygen, iron and other nuclei synthesized in stars, the secondaries that reach the ground level are muons (μ^-), nucleons (p, n), electrons (e^-), neutrinos (ν_μ), and their anti–particles ($\mu^+, e^+, \overline{\nu_\mu}$).[4] Since Cherenkov radiation is only created by charged particles, only the μ^-, p, and e^- intensities must be understood in detail. The intensity of each of these particles directly depends on the primary particle's momentum (energy).

Muons are the most abundant charged particles at ground level and the majority of cosmic ray measurements have centered on muons in the energy range between 0.2 and 1000 GeV/c. Around 1 GeV/c the proton intensity is about 3.5%

---

[4]From this point on, anti–particles will be assumed included when reference is made to the particles in the context of cosmic rays.

of the muon intensity. But it drops to about 0.5% as the momentum increases to 10 GeV/c. Electrons on the other hand only become significant in intensity at momentum levels near 10 MeV/c, where the electron intensity exceeds the muon intensity. The electron intensity quickly drops to about 1.1% as the momentum increases to 1 GeV/c [6]. The graph and table in figure 3 show the intensity distri-
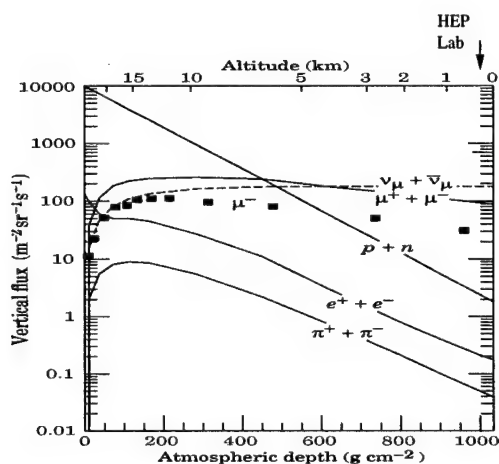
Energy (GeV/c)	Intensity $(m^2\ sr\ s(GeV/c))^{-1}$			Ratios	
	μ^A	p^B	e^C	p/μ^C	e/μ^D
.01			30		
0.2	12		6		50%
1.0	17.7	6.195×10^{-1}	0.2	3.5%	1.1%
10.0	4.14×10^{-1}	2.1×10^{-3}		0.5%	
100.0	1.5×10^{-3}				

Figure 3: Top – Graph of vertical fluxes of cosmic rays with $E > 1$ GeV/c [6]. The altitude of the HEP Lab at the University of Virginia is indicated on the graph. Bottom – Table of intensities and ratios of charged particles at various energies. A: Data from an experiment in Fort Sumner with an apparatus referred to as CAPRICE97 ($\theta = 9^o$) [7]. B: Determined from applying muon data to ratio p/μ. C: Data(e) and ratio (p/μ) given by the Particle Data Group [6]. D: Determined by comparing data for μ and e.

butions discussed above. In order to understand which energies are significant for

Particle Type	Cherenkov Threshold Kinetic Energy (MeV/c)
e	0.268
μ	55.51
p	492.97

Table 1: Cherenkov threshold kinetic energies for different charged particles.

each type of particle, the Cherenkov threshold kinetic energies in $NaBi(WO_4)_2$ for each type of particle are listed in table 1.

Additionally the charged particle intensity depends on the angular distribution of the zenith angle (θ)of the incident particle. For muons with momentum of near 3 GeV/c, the angular distribution is proportional to $cos^2\theta$, while the distribution is steeper for lower momentum and it flattens to $sec\theta$ for momentums greater then 10 GeV/c and θ less than 70° [6].

The intensity of charged particles does have some dependence on altitude and location on the earth. Of course the more atmosphere the particles go through increases the chance for interactions or decays to occur. But there is limited differences of intensity for muons at altitudes within a kilometer of sea level. Also the effects of the location on the earth on intensity for muons are also minor.

More details on the charged particle intensity at ground level will be addressed during the Monte Carlo simulation in section 3.

2.2   Detector $\{NaBi(WO_4)_2\}$ Characteristics / Design

The samples of $NaBi(WO_4)_2$ available for study were three cubes with dimensions, 22 x 22 x 22 mm, and one rectangular piece with dimensions, 22 x 22 x

Property	Published Quantity	Measured Quantity
$Density(g/cm^3)^A$	7.58	$7.45 \pm .02$
$Refractive\ Index^A$	2.15	$2.18 \pm .1$
$Rad\ Length(cm)^A$	1.04	*
$Rad\ Hardness(rad)^B$	10^7	*

Table 2: Properties of $NaBi(WO_4)_2$. A – published in [8]. B – published in [2]. * – properties not measured.

100 mm. The crystals have a yellow tint and are sensitive to sudden temperature changes, one cubic sample formed a massive internal crack when placed in chilled water from a water fountain. The basic properties of the material were measured independently and compared with published data on the material. The density was determined by measuring the weight of the material with a digital scale in air and in water then calculating as such, $\frac{W_a}{W_a - W_w} = \frac{\rho}{\rho_w}$. The index of refraction (taken to be independent of wavelength) was measured by transmitting white light, which was collimated by using a slit box, through the rectangular piece and applying Snell's Law (equation 18).

$$n_1 sin\theta_1 = n_2 sin\theta_2 \tag{18}$$

As stated before, these independent measurements were in good agreement with the previously published values. Table 2 gives a listing and values of various properties of $NaBi(WO_4)_2$.

One property of $NaBi(WO_4)_2$, besides the refractive index, that will be very important in the Monte Carlo simulation is the attenuation length of the material. In order to compute the optical attenuation length, the optical transmission

coefficient must be known or measured as a function of wavelength. Equation (19) below gives the measured or attenuated transmission coefficient (T_A) for a photon as a function of the unattenuated transmission coefficient (T_0), thickness of the material (t), and the attenuation length (λ).

$$T_A = T_0 e^{-\frac{t}{\lambda}} \qquad (19)$$

While t is known in the equation above, we must measure T_A for each wavelength of interest and compute T_0 in order to determine λ. In order to compute T_0, we must first examine the behavior of electromagnetic waves in nonconducting media. By determining how the electromagnetic fields of the wave are modified at the interface of two media will enable us to compute T_0. First we begin by applying the electrodynamic boundary conditions (equations 20) for linear media to an incident plane wave.

$$\left.\begin{array}{rclcrcl} \epsilon_1 E_{1\perp} &=& \epsilon_2 E_{2\perp} & & E_{1\parallel} &=& E_{2\parallel} \\ B_{1\perp} &=& B_{2\perp} & & \frac{1}{\mu_1} B_{1\parallel} &=& \frac{1}{\mu_2} B_{2\parallel} \end{array}\right\} \qquad (20)$$

For measurements of the attenuation length, the incident wave is normal to the surface so there are no components perpendicular to the surface ($E_\perp = B_\perp = 0$). This development was only used for measurement of the attenuation length, more complicated formulas (with dependence on the incident angle) were applied when creating the Monte Carlo simulation. A plane wave traveling in the positive x direction and polarized in the positive y direction is depicted in figure 4 and has electric and magnetic fields as in equations (21) [9] below.
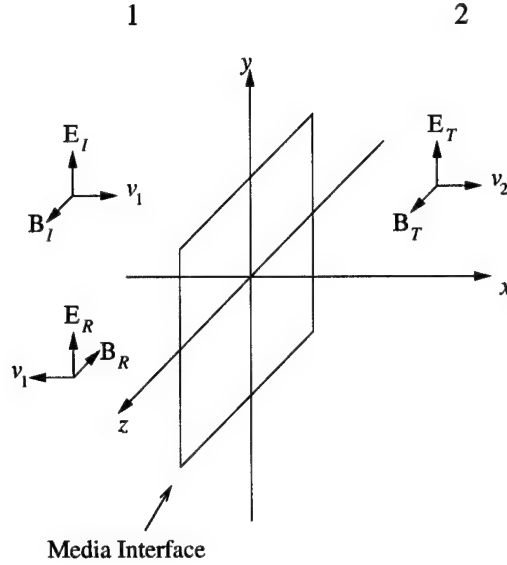
Figure 4: This picture shows the respective electric and magnetic fields for the incident, reflected, and transmitted waves of a plane wave normal incident to the surface of linear non-conducting media.

$$
\left.\begin{array}{rl}
E_I(x,t) & = E_{0_I} e^{i(k_1 x - \omega t)} \hat{j} \\
B_I(x,t) & = \frac{1}{v_1} E_{0_I} e^{i(k_1 x - \omega t)} \hat{k}
\end{array}\right\} \tag{21}
$$

Of course the incident plane wave will give rise to a reflected (equations 22) and transmitted (equations 23) plane wave as well [9].

$$
\left.\begin{array}{rl}
E_R(x,t) & = E_{0_R} e^{i(-k_1 x - \omega t)} \hat{j} \\
B_R(x,t) & = -\frac{1}{v_1} E_{0_R} e^{i(-k_1 x - \omega t)} \hat{k}
\end{array}\right\} \tag{22}
$$

$$
\left.\begin{array}{rl}
E_T(x,t) & = E_{0_T} e^{i(k_2 x - \omega t)} \hat{j} \\
B_T(x,t) & = \frac{1}{v_2} E_{0_T} e^{i(k_2 x - \omega t)} \hat{k}
\end{array}\right\} \tag{23}
$$

By applying the boundary conditions above to the plane waves, we can determine

the reflected and transmitted amplitudes in terms of the incident amplitude as given below (assuming that $\mu_1 = \mu_2 = \mu_0$, as is the case for most media).

$$E_{0_R} = \left| \frac{v_2 - v_1}{v_2 + v_1} \right| E_{0_I}, \qquad E_{0_T} = \left(\frac{2v_2}{v_2 + v_1} \right) E_{0_I} \qquad (24)$$

Equation (24) can be expressed in terms of the refractive index as shown below since $v = \frac{1}{\sqrt{\epsilon \mu}} = \frac{c}{n}$.

$$E_{0_R} = \left| \frac{n_1 - n_2}{n_1 + n_2} \right| E_{0_I}, \qquad E_{0_T} = \left(\frac{2n_1}{n_1 + n_2} \right) E_{0_I} \qquad (25)$$

From the amplitude of the plane waves, we can compute the transmission coefficient (T), as shown in equation (26), through the interface of the linear media by determining the ratio of the transmitted intensity (I_T) to the incident intensity (I_I) where the intensity is, $I = \frac{1}{2} \epsilon v E_0^2$ [9].

$$T = \frac{I_T}{I_I} = \frac{\epsilon_2 v_2}{\epsilon_1 v_1} \left(\frac{E_{0_T}}{E_{0_I}} \right)^2 = \frac{n_2}{n_1} \left(\frac{2n_1}{n_1 + n_2} \right)^2 \qquad (26)$$

Notice that the expression for T is symmetric in n_1 and n_2, so that the transmission coefficient is the same whether entering or exiting a material $(T_{1 \to 2} = T_{2 \to 1})$ and since n is assumed to be independent of λ, T is independent of λ as well. Now that we have an expression for the transmission coefficient at one interface, we can compute the unattenuated transmission coefficient (T_0) by applying T at each interface of the cube. It is also important to take into account two reflections inside the cube as it will contribute to the overall transmission coefficient. The resulting output after considering more than two is so small that it does not sig-

nificantly contribute to the overall transmission coefficient. Figure 5 shows how $T_0 = TT + TTRR$ is computed from the coefficients from each interface, where
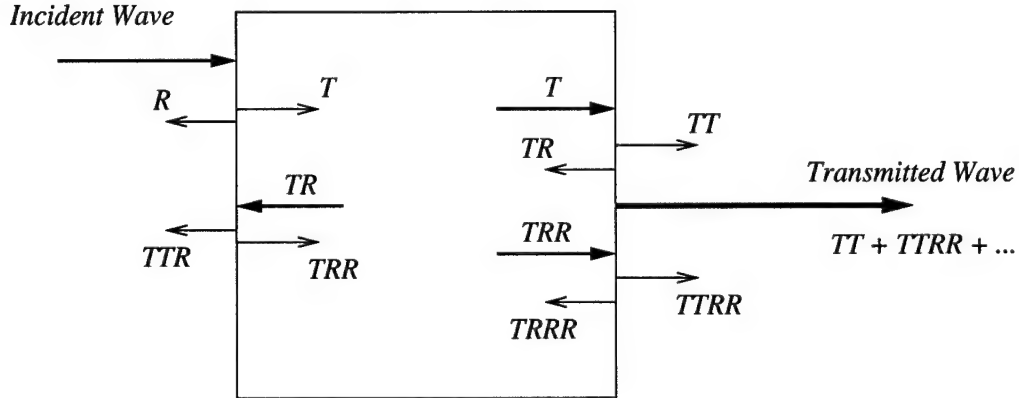
Figure 5: Visual depiction of how resulting T_0 is computed from transmission coefficient for each interface in the test setup.

$R = (1 - T)$ and terms greater than the second have been dropped.

Except for one study of the radiation hardness of the material, there is limited data published on the transmission of radiation through $NaBi(WO_4)_2$ [2]. So in order to accurately determine T_A and consequently the attenuation length (λ) for various wavelengths, a Cary 5E (500 series) UV-Vis-NIR Spectrophotometer made by Varian, Inc. (see figure 6) was used. This spectrophotometer is a PC controlled system with the following specifications: a wavelength range of 175-3300 nm, a double beam configuration, the capability to measure absorption or transmission, and null sample baseline subtraction capability.

Prior to taking measurements with the spectrophotometer, all samples were carefully cleaned with optical grade methanol. The spectrophotometer was set up in a double beam and reduced slit configuration. The reduced slit was cho-
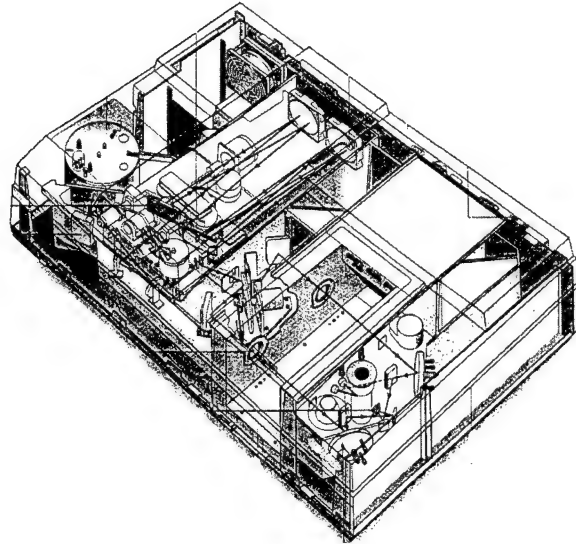
Figure 6: Cary 5E Spectrophotometer.

sen to ensure that the beam of transmitted light was smaller than the sample size. Just prior to each actual measurement, a baseline measurement was taken with the sample chamber empty. Once the baseline was recorded, the sample was positioned and measured. The Cary spectrophotometer automatically subtracts the baseline from the actual measurement, thus giving the true attenuated transmission coefficient. Two samples, 22 mm and 100 mm, were measured over a range of wavelengths from 350 nm to 800 nm. One data point was recorded for each nanometer in the stated range, thus giving a total of 451 data points per sample. Once T_A was measured, the attenuation length was computed for each wavelength using equation (19) from above. The attenuation length was measured using the rectangular sample with the thickness of 100 mm. This attenuation length was then used to predict the attenuated transmission coefficient

for the cube (thickness 22 mm). The excellent agreement between measured and predicted T_A for 22 mm of thickness is shown in figure 7 for wavelengths ranging from 400–650 nanometers. Based on these reliable results, the attenuation length measured from the 100 mm sample as a function of wavelength was used in the Monte Carlo simulation, see figure 8. This range was chosen due to the fact that the attenuation length below 400 nm is less than 10mm and the cathode sensitivity of the PMT does not go beyond 650 nm. The graph in figure 7 also shows T_A for the 100 mm sample. The dependence of the transmission coefficient on
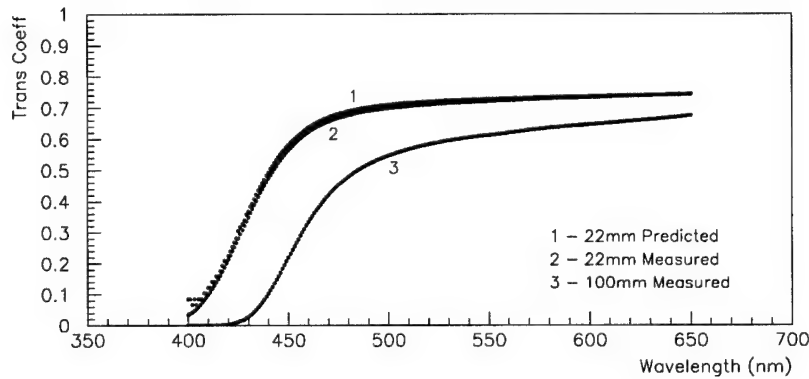
Figure 7: T_A measured for 22 mm,100 mm and predicted for 22 mm. The predicted curve was determined by applying λ measured for the 100mm sample and using equation (19) to compute T_A for the 22 mm sample. The graph shows excellent agreement between measured and predicted T_A for 22 mm thickness, except for wavelengths near 400nm where the attenuation length is on the order of 10mm.

the wavelength is also easily seen, especially in the range of 400-500 nm. The measurements taken with the spectrophotometer are is excellent agreement with the study on radiation hardness of $NaBi(WO_4)_2$ [2] presented in figure 9.
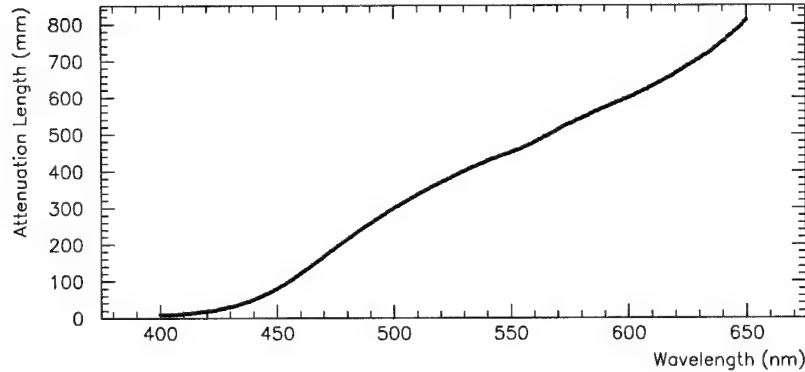
Figure 8: The attenuation length for photons in $NaBi(WO_4)_2$ as a function of wavelength measured using the Cary 5E Spectrophotometer.

2.3 PMT Specifications

The photomultiplier tube used for light collection while taking data from the $NaBi(WO_4)_2$ was a Hamamatsu Metal Package PMT R7400U Series [10]. All data presented in this thesis was taken with the R7400U model operating at 920 volts. It is a standard bialkali cathode PMT that is 16 mm in diameter and has a length of 12 mm (not including the pins). The window is made of borosilicate glass, which has a refractive index of 1.473, and is 9.5 mm in diameter. The cathode of the PMT is actually on the inner surface of the glass of the window. Its spectral response ranges from 300 nm to 650 nm, with a peak wavelength of 420 nm. A graph of the spectral response of the cathode and the gain of the PMT are shown in figure 10.

2.4 Data Acquisition Setup

The primary purpose of the PMT is to convert photons to photo–electrons, thus the charge produced by the PMT is proportional to number of photons. In order
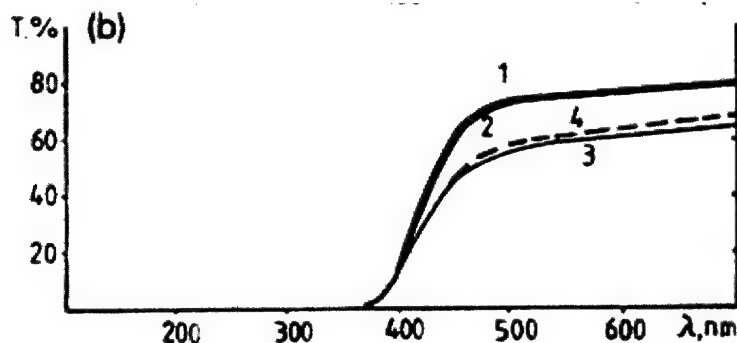
Figure 9: Per cent transmission ($100*T_A$) for $NaBi(WO_4)_2$ with thickness of 10 mm. Each curve corresponds to the following conditions, 1: before irradiation, 2: after dose of 10^7 *rad*, 3: after dose of 10^8 *rad*, and 4: 50 days of recovery [2].

to determine the output of the PMT when a charged particle traveled through the $NaBi(WO_4)_2$ detector, a computer based data acquisition system running CAMAC was setup. The system was used to record the charge produced by the PMT in a variety of configurations, detector coatings, and detector surface conditions. A cosmic ray telescope was designed using two scintillators as a double coincidence to form the trigger and $NaBi(WO_4)_2$ as the detector placed between them. The scintillating trigger counters, with dimensions 17.5 x 17.5 x 10.0 mm, were fixed to lucite light guides using epoxy and the light guides were connecting to PMTs (a different type of PMT than that used with the $NaBi(WO_4)_2$ detector). All of the telescope configurations, shown in figure 11, were enclosed in a light–tight box with a thin copper sheet covering the entire box.

The output signals of the PMTs were directed through numerous electronic modules, as seen in figure 12. The scheme of the logic is mostly self evident from the diagram, but here are a few points of interest. The threshold on the
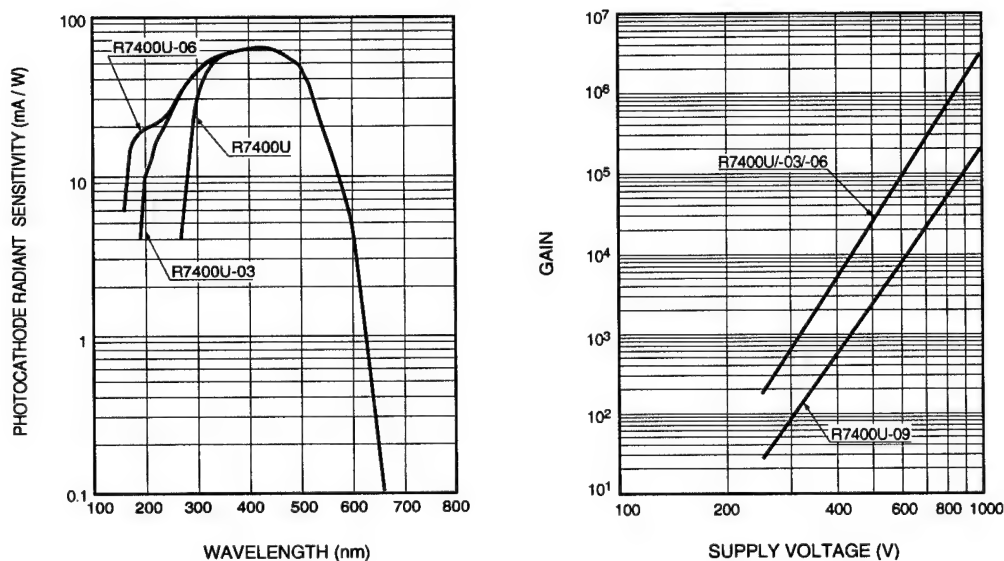
Figure 10: Typical spectral response (Bialkali) and typical gain characteristics for PMT R7400U.

discriminators (items 4 & 12 in figure 12) was set to 30 mV, so only pulses greater than 30 mV would cause the discriminator to produce an output pulse of fixed height and width. If the AND gate (item 6 in figure 12) in the logic unit received coincident pulses from the scintillators within 10 ns, then the trigger was satisfied and the logic unit produced an output pulse. The latch (item 9), which was fabricated at the University of Virginia for a previous experiment, was used to ensure that only one event was recorded at a time and provided a strobe to the I/O unit (item 8), a 75 ns gate to the ADC (item 13), and a common start for the TDC (item 10). The program controlling the crate of electronics continuously polled the I/O unit to determine if it had been strobed. Once the I/O unit was strobed, the program would read and clear the ADC and TDC. A calibration pulse was also used to determine and record the value of the pedestal for the ADC. In order to ensure the pulses from the PMTs reached the ADC and
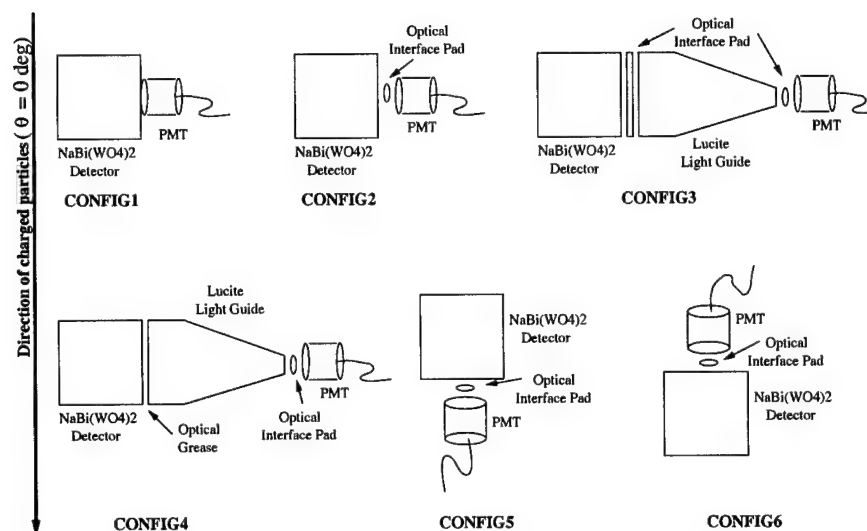
Figure 11: Various setup configurations used when taking data with $NaBi(WO_4)_2$. The optical interface pads are transparent and made from a GE Silicone/RTV-615.

TDC in time with the gate, long wires were used to delay the signals going to the ADC and TDC.

The data acquisition system as described above worked well and was used to record all of the data for the $NaBi(WO_4)_2$ detector. A normal run would typically consist of roughly 2000–3000 events (particles) and the data recorded by the ADC and TDC was analyzed as discussed in section 4.
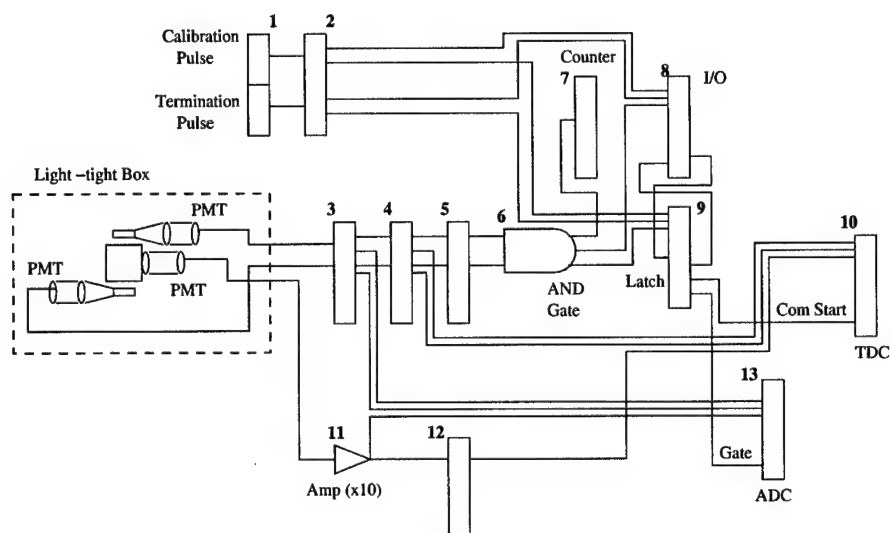
Figure 12: Diagram of the Data Acquisition Setup. 1: Phillips Scientific 794 Gate / Delay Generator; 2: Ph Sci 755 Quad Four Field Logic Unit, 3: Ph Sci 740 Linear Fan-Out; 4: LeCroy 623B Octal Discriminator; 5: Ph. Sci, 726 Digital Fan-Out; 6: Ph Sci 755 Logic Unit; 7: CAEN Counter; 8: CAEN I/O Register; 9: Fabricated Latch; 10: LeCroy 2228A TDC; 11: LeCroy 612A PM Amp (x10); 12: LeCroy 620D Discriminator; 13: LeCroy 2249A ADC.

3 Monte Carlo Simulation

The Monte Carlo simulation developed for this thesis was coded using Fortran 77 and run on DEC3000 servers located in the High Energy Physics Group at the University of Virginia. This Monte Carlo simulation models the manner in which cosmic rays produce Cherenkov radiation in $NaBi(WO_4)_2$, traces those photons through the cubic detector and its interfaces, and determines the number of photo–electrons produced in the PMT. Various simulations have been done for the various detector configurations and PMT interfaces studied and have been compared with the data. The comparison of Monte Carlo vs data will be discussed in section 4.

3.1 Cosmic Ray Distribution of Charged Particles at Ground Level

As described before, the basic configuration of the cosmic ray telescope was to position a trigger counter made of scintillator above the $NaBi(WO_4)_2$ cube and another scintillating trigger counter just below the cube. This setup was replicated in the simulation by geometrically centering the trigger counters above and below the cube with the surfaces touching each other. Any variation in the positioning of the trigger counters in the actual setup was minor and had minimal effect on the cosmic ray spectrum satisfying the trigger. This was tested by varying the position in the Monte Carlo simulation and examining the affect on the results. The results were unaffected by the positioning, except for a slight shift in the extreme cases were the trigger counters were placed at opposite corners of
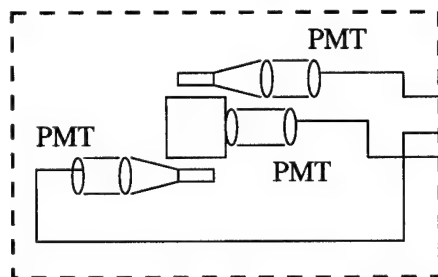
Figure 13: Diagram of the Data Acquisition Setup.

the detector. It would have been obvious if such positioning had occurred in the actual setup.

In order to reproduce the cosmic ray spectrum and determine if the double coincidence trigger is satisfied, first points on the top trigger counter are randomly selected. From these points random three dimensional unit vectors are produced using the standard CERN library subroutine, RN3DIM. Assuming that all rays are traveling downward, only one hemisphere of vectors are kept - all others are disregarded. Thus each angle of incidence is as likely as any other and does not bias to angles closer to the vertical. Now that there is a random vector passing through a point in the top trigger counter, the vector is extended downward through the cube to determine if the second trigger counter is hit. If the second trigger is satisfied, then the ray is kept and the trajectory through the cube is recorded (entry and exit points along with angle θ). If the second trigger is not satisfied, then the event is disregarded.

Under this method an angular distribution for the zenith angle (θ – the angle measured with respect to the vertical), prior to trigger verification, ranges from

0°–90° and is peaked at 90° as expected since the surface area on the sphere is much greater about an angle of 90° than about 0°. After the trigger verification, the distribution ranges from 0° to near 45° with a peak about 22°–23°. The largest possible angle for the charged particle, yet still satisfying the trigger, based on the geometry described above is 48.36^o.

As addressed in section 2.1, the intensity varies as a function of zenith angle, but this function changes for different ranges of momentum or energy of the charged particle. The three general ranges of the momentum for which the angular variation is measured are: ≤ 2 GeV/c, 2–10 GeV/c, and ≥ 10 GeV/c. Review of Particle Physics explicitly gives the dependence of the intensity on θ for medium and high values of momentum , but the dependence for low momentum is only given qualitatively, describing it as steeper [6]. The limited data published on cosmic rays, especially for energies below 1 GeV/c and various values of θ, creates uncertainty in determining the muon intensity as a function of momentum and zenith angle. In order to determine the dependence of intensity on zenith angle and assuming it can be represented as a function of the form $cos^n\theta$, data from the CAPRICE97 experiment [7] was used to predict the intensity at large values of θ and momentum under 2 GeV/c. Fitting the predicted intensity to theoretical models by Naumov [11] and maintaining the general integrity of the original curve, n was determined to be on the order of 5. With the θ dependence determined for all momenta ranges (summarized in table 3), the data from CAPRICE97 was used to determine the intensity for all momenta and θ values up to 50° (see figure 14). Once the distributions have been created for all ranges of angles, the next step in the simulation is to assign a uniformly random momentum to each track of a

Momentum (GeV/c)	Function
≤ 2	$cos^5\theta^A$
2–10	$cos^2\theta^B$
≥ 10	$sec\theta^B$

Table 3: Intensity as a function of θ over various momentum ranges. A: Fit to the theoretical models by Naumov [11] and CAPRICE97 experiment [7]. B: Review of Particle Physics citepdg.

charged particle and weight that track according to the distributions shown in figure 14. The weight determines whether that track is kept or not. After this is done the resulting distribution is determined not only by the geometry of the setup, but also by the dependence on θ.

The distribution of cos(zenith) after weighting and before the geometric trigger verification is displayed in figure 15. Additionally, the distribution after both the intensity weighting and the geometric trigger is also displayed. The Monte Carlo simulation allows for a maximum zenith angle of 48° and a momentum range of $0.01 - 100$ GeV/c. While the momentum spectrum of muons is generally understood for energies above 1 GeV/c, the spectrum below 1 GeV/c is not. With very little published data for energies below .2 GeV/c, the intensity in this region was extrapolated from the curves presented in figure 14.

With the momentum in hand the last aspect of the particle that must be determined is β. Evident from equation (27), the mass of the particle must be known to determine β.

$$\beta = \sqrt{1 - \frac{m^2c^4}{p^2c^2 + m^2c^4}} \qquad (27)$$

The possible charged particles, as stated in the table in figure 3, are e, p, or μ.
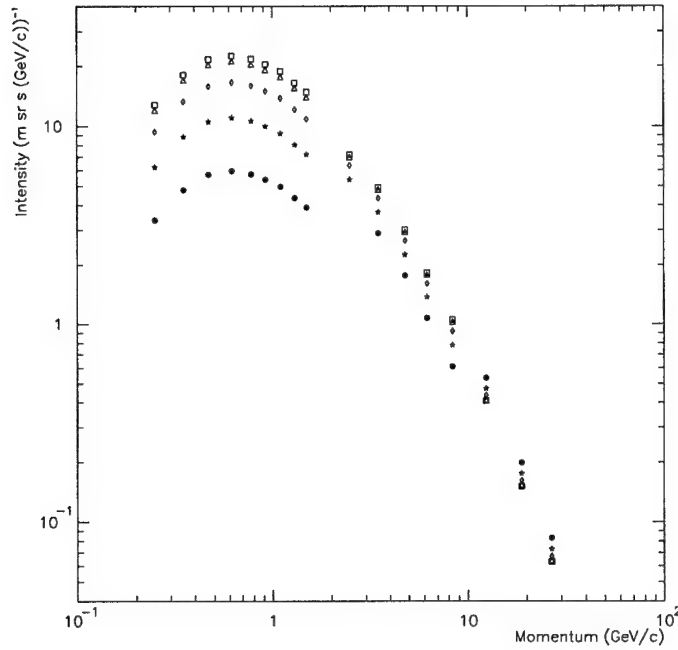
Figure 14: Graph showing intensity as a function of momentum for various values of θ. All curves predicted by applying the functions from table 3 to the data from CAPRICE97 experiment [7] which is curve, $\triangle$. Distributions are discontinuous due to applying separate functions over total momentum range. Each curve is used for a range of angles when applied in the Monte Carlo simulation: $\square$ – (0°–5°), $\triangle$ – (6°–15°), $\diamond$ – (16°–25°), $\star$ – (26°–35°), and $\bullet$ – (40°).

Electrons make up the low end of the energy spectrum for cosmic rays at ground level. They begin to require consideration at energies 1 GeV/c and below. The flux due to this type of particle is eliminated by the physical location of the detector setup. As described in section 2, the building where the detector was located has a one foot thick reenforced concrete roof, and the detector was located in a wood framed light–tight box with 1 mm of copper sheeting covering the entire surface. Additionally, to ensure that the electrons were eliminated a test was conducted by taking a run of data with a stack of lead bricks on top of the light box. The lead was 100 mm thick covering most of the possible angular
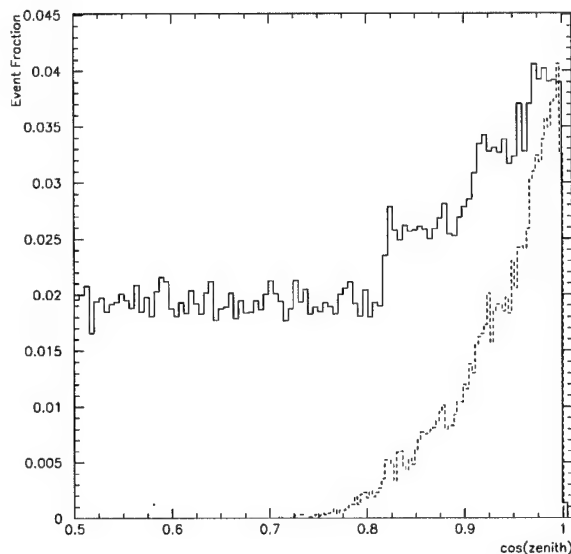
Figure 15: The solid histogram shows the distribution of cos(zenith) after weighting according to curves in figure 14 and prior to applying the geometry of the trigger. The dashed histogram displays the distribution of accepted events after applying both geometry and intensity weight.

distribution and 50 mm thick for the most extreme angles possible. Figure 16 shows the ratio of the histograms taken for the two runs with the exact same setup, except for the addition of the lead in one run.

The ratio of the proton intensity to the muon intensity is only 0.5% at 10 GeV/c and increases to 3.5% at 1 GeV/c [6]. Again the lead test should eliminate the proton as a possible particle type. The protons with higher energy would interact in the lead and cause the production of pions and thus change the distribution seen from the detector. If the protons were low enough in energy not to interact, then they would lose too much energy in the lead according to the Bethe–Bloch [6] equation (28) and would no longer have a β high enough to
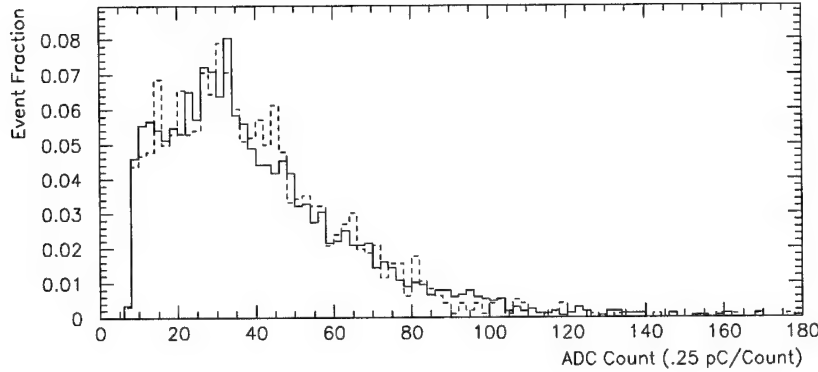
Figure 16: Normalized histograms comparing data recorded with and without lead bricks above the light tight box. Without Lead – solid. With lead – dashed.

produce Cherenkov photons.

$$\left(-\frac{dE}{dx}\right) \;=\; Kz^2\frac{Z}{A\beta^2}\left[\frac{1}{2}\,ln\frac{2m_ec^2\beta^2\gamma^2T_{max}}{I^2} - \beta^2 - \frac{\delta}{2}\right] \tag{28}$$

(In the equation above the variables are defined as follows: $K = 4\pi N_A r_e^2 m_e c^2$, N_A = Avogadro's number, r_e = classical electron radius, m_e = electron mass, Z = atomic number of medium, A = atomic mass of medium, $\beta = v/c$, $\gamma = \left(\sqrt{1-\beta^2}\right)^{-1}$, T_{max} = max kinetic energy imparted to free electron in single collision, I = mean excitation energy, and δ =density effect correction to ionization energy loss.) The minimum β required to produce Cherenkov radiation in $NaBi(WO_4)_2$ is .46511, which corresponds to a proton energy of about 493 MeV/c. So after examining the possible particles, it can be concluded with confidence that almost exclusively the only type of particles passing through the detector are muons, thus electrons and protons are ignored in the simulation.

With the particle type identified, β can be determined for each particle based

on that particle's momentum. Now all required elements are known about the particle in order to determine the Cherenkov photons emitted.

3.2 Cherenkov Photon Distribution and Tracking Through All Interfaces

From this point the simulation focused on constructing the number of and manner in which Cherenkov photons are emitted. Recalling equation (14) the number of Cherenkov photons produced per unit length is given.

$$\left(\frac{d^2N}{dxd\lambda}\right) = \frac{2\pi\alpha Z^2}{\lambda^2}\left(1 - \frac{1}{\beta^2 n^2(\lambda)}\right) \tag{29}$$

Using the trajectory of the particle to determine the total distance traveled by the particle in the detector, the trajectory is then segmented into 5 mm sections, with a remainder section of less than 5 mm at the bottom of the detector. Using equation (29), the number of photons emitted per section per wavelength are determined for wavelengths from 400–650 nm. It is important that the photons are generated as a function of wavelength, since the attenuation length of photons in $NaBi(WO_4)_2$ depends on wavelength as discussed in section 2.2. Initial position and direction of each photon are determined along the trajectory of the charged particle. The initial momentum vector is constrained to lie on a cone with vertex angle corresponding to the Cherenkov angle which also depends on β as given in equation (30) below.

$$\theta_c = cos^{-1}\left(\frac{1}{\beta n}\right) \tag{30}$$

The angle (θ_c) is with reference to the particle's trajectory and the momentum vector is randomly distributed azimuthally on the cone. Again this process is repeated individually for each photon emitted.

Now that the photon has an initial position and momentum vector, it is tracked as it moves in the detector. The photon is traced to the nearest surface and once it reaches a surface several possibilities arise depending on the configuration and properties of the medium at that surface. The first possibility to be checked is to see if the photon has traveled further than its maximum distance allowed. The maximum distance is an exponential distribution of the attenuation length. If the maximum distance has been exceeded then the photon is absorbed and the next one is emitted and tracked as above.

If the photon has not been absorbed, the interactions of the photon with the surface must be determined according to the angle of incidence and the properties of that surface, such as refractive index of the medium on either side of the surface and whether the surface is absorbing, reflecting, transmitting, or diffusely reflecting. All these factors are taken into account given the current configuration and geometry of the system. Additionally if the photon is reflected or transmitted, the proper change in the photon's momentum vector is computed based on the incident angle, the normal to the surface, and refractive indices of media. Once the new direction is determined, the photon is tracked until it intersects with the next surface. The same process is applied as before to determine the photon's actions at that surface.

As stated above, the interactions of the photon with the surface depend on the configuration, the geometry, and the coatings for the surfaces. The $NaBi(WO_4)_2$

cubes were covered in two different materials: aluminium foil and reflecting paint. The majority of the data was taken with all surfaces covered with a reflecting aluminium foil .01 mm thick. The only surface which was not completely covered was the one where the PMT was placed. On this surface a circular hole was cut in the foil with a diameter equal to that of the PMT window (9.5 mm). Although there will always be some air gaps, this coating was first simulated as if the foil were pressed firmly against the $NaBi(WO_4)_2$ without allowing any gaps of air. So all photons incident on one of these surfaces, smooth surface covered with aluminium foil, were assumed to be perfectly reflected. In order to test the effect of air gaps between the cube and the foil wrapping, simulations were conducted in which a small gap of .25 mm was inserted between the cube and the foil. There was little to no affect on the resulting distribution for number of photo–electrons produced. Based on these results, the primary factor governing the interactions at the surface is the small critical angle ($\theta_{crit} = 27.7^o$ for $NaBi(WO_4)_2$ – air).

Additional data was taken using reflecting paint as a covering on all surfaces. The surface with the PMT was covered only on the portions surrounding a circular region the size of the PMT window, just as with the foil. Again the assumption was made that there were no significant air gaps between the surface of the cube and the paint. But the property of the paint is such that the photons are reflected diffusely, so the simulation also reflected the photons diffusely.

Thus, the reflection of photons have been simulated for both types of coatings and for all surfaces except the most important, the surface with the PMT. The behavior of this surface is more varied and complex since data was collected under various configurations from the simplest, CONFIG 1, to the most complex,

CONFIG 4. Additionally the condition of the surface itself was varied: smooth or rough. It was either smooth (as from the manufacturer) or roughed by the application of 400 grit sandpaper. The simulation of the rough surface will be addressed before dealing with the different configurations. Originally the surface was roughed in an attempt to vary the incident angle of the photons by varying the normal to the surface in order to allow a greater percentage of light to be transmitted out of the cube. The modeling of this surface is not straightforward.

In order to model the rough surface, Spectra-Physics HeNe, 3 mW laser light
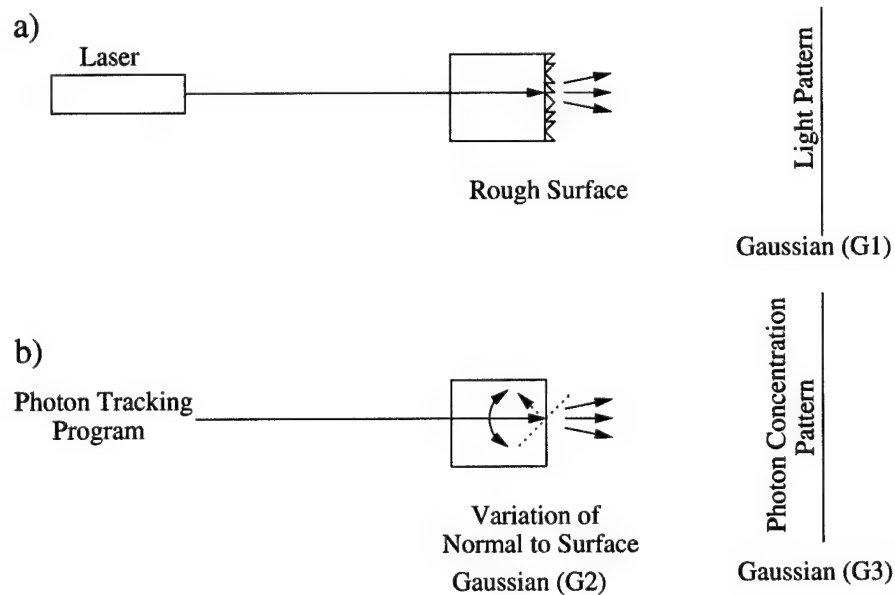
Figure 17: Diagram showing the method used to model the rough surface of the cube. a) The laser light pattern was fit to a Gaussian function (G_1). b) Many photons were tracked with perpendicular incidence to the surface, but the normal was varied according to a Gaussian function (G_2). The resulting photon concentration was fit to a Gaussian function (G_3). The σ of G_2 was varied until the σ of G_1 matched that of G_3.

was directed through the cube, normal to a smooth surface and exiting through the rough surface (see figure 17). The resulting pattern of the laser light was

measured on a plane positioned 77 mm from the cube. The normal aperture of the laser had to be masked with a piece of black cardboard with only a pin–hole for the laser light to pass through. This was required since the normal aperture of the laser produced a beam that was too large and resulted in a triple peaked distribution. The intensity of the light was measured at positions of 2.5 mm apart
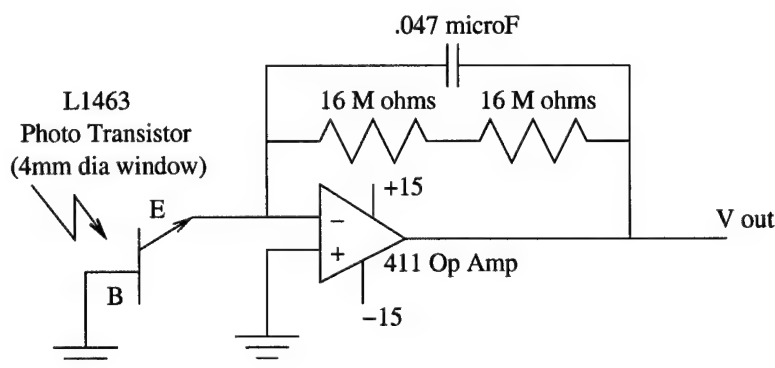
Figure 18: Circuit used to measure the intensity of the laser light at different points. It is a high gain circuit that converts the light into voltage to be measured with an oscilloscope. Basic circuit design taken from Hayes and Horowitz electronics lab manual [12]

across a horizontal width of nearly 80 mm in a dark room using a phototransistor as a photodiode and the circuit in figure 18, which converted the laser light into voltage. A Gaussian function (G_1) was fit to the pattern of the laser light. Using the photon tracking program, many photons were directed perpendicular to the surface of the cube. As each photon intersected the surface, the normal to the surface was varied as a Gaussian function (G_2) and the resulting photon concentration on a plane 77 mm away was recorded. This photon concentration pattern was also fit to a Gaussian function (G_3). To best model the surface, the σ of G_2 was changed until the σ of G_3 matched that of G_1. The histogram for

Figure 19: Histogram displaying the laser light intensity data (solid) and the photon concentration data (dashed). The normal to the surfac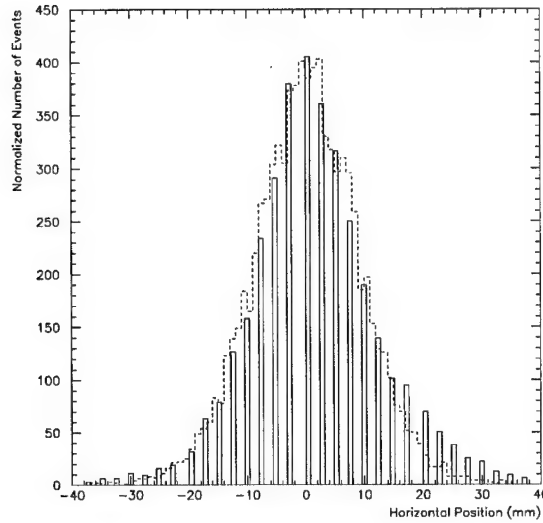e was varied according to a Gaussian function with $\sigma = .0988$ radians to create the photon concentration histogram.

the laser light intensity data and the photon concentration are shown figure 19. Based on these findings, the rough surface was modeled by varying the normal to the surface as a Gaussian distribution, with $\sigma = .0988$.

So in the full Monte Carlo when a configuration was used with the rough surface, the interactions of the photons with that surface were modeled as described above. Having addressed the coating of the cube and the conditions of the surface of the cube with the PMT, the last aspects of the Monte Carlo to take into account were the configurations. The primary concern for the modeling of the configurations was the refractive index for the media on either side of each interface. As shown in section 2.2, the transmission coefficient for electromagnetic radiation (photons) depends on the refractive indices, but it also depends on the incident angle when θ is other than 0°. The coefficients, presented here without derivation [9], are more complicated and are separated into components

corresponding to whether the photon is polarized parallel or perpendicular to the plane of incidence [5] as given in equations(31).

$$T_\parallel = \alpha\beta\left(\frac{2}{\alpha+\beta}\right)^2 , \qquad T_\perp = \alpha\beta\left(\frac{2}{1+\alpha\beta}\right)^2 \left.\vphantom{\begin{array}{c}1\\1\\1\\1\end{array}}\right\}$$
$$\alpha = \frac{\sqrt{1-\left(\frac{n_1}{n_2}sin\theta_i\right)^2}}{cos\theta_i} , \qquad\qquad \beta = \frac{n_2}{n_1} \qquad\qquad (31)$$

From equations (31) it is apparent that the polarization of the photon must be considered when determining the transmission probability at an interface. As noted in section 1.2, Cherenkov radiation is linearly polarized in the plane formed by the emitted photon and the charged particle. This is not necessarily the same plane as the plane of incidence and in general is not. The Monte Carlo simulation treats the polarization of each photon by averaging the perpendicular and parallel coefficients to determine the resulting coefficient. This simplification is justified for a number of reasons. First the trajectory of the particle is not fixed and only restricted by the geometry and cosmic ray intensity spectrum. From these various tracks, the photons are emitted azimuthally random on the Cherenkov cone governed by the momentum of the particle. Another factor which smears the photon polarization is that a photon which enters the PMT has reflected from an average of 13 (CONFIG 1-2) or 25 (CONFIG 5-6) surfaces prior to reaching the PMT. The last factor supporting the averaging of the photon polarization is that several simulations were conducted with the transmission coefficient set to that of the parallel polarized photon with no change resulting in the charge

---

[5]A plane formed by the incident, reflected, and transmitted wave vectors.

Medium	Refractive Index
$NaBi(WO_4)_2$	2.15
Borosilicate Glass (PMT)	1.473
Lucite	1.49
Optical Grease	1.465
Optical Interface Pads	1.406

Table 4: List of refractive indices for various materials used in setup.

spectrum.

A summary of the refractive index for each material used is listed in table 4. Configurations which require additional detailed explanation are those that have the lucite light guide as a component.

The light guide was introduced as a material to match refractive indices and also transition from the square surface of the cube to the round surface of the PMT window. The lucite light guide was constructed with a square surface on one end which was the same size as the surface of the cube, which gradually changed into a conical shape with decreasing diameter until it was the size of the PMT window. The total length of the light guide was 5 cm and was also completely coated in foil. A picture of the lucite light guide is shown in figure 20. It was initially believed that the light guide would enable more photons to be collected in the PMT since without it all photons in the cube hitting the surface outside of the circular region of the PMT are reflected back into the cube. This assumption turned out to be false as seen in the data presented in section 4. In order to study this, the geometry of the light guide was put into the photon tracing program where photons were initialized at the square end with a random momentum vector directed into the light guide. A detailed examination of the
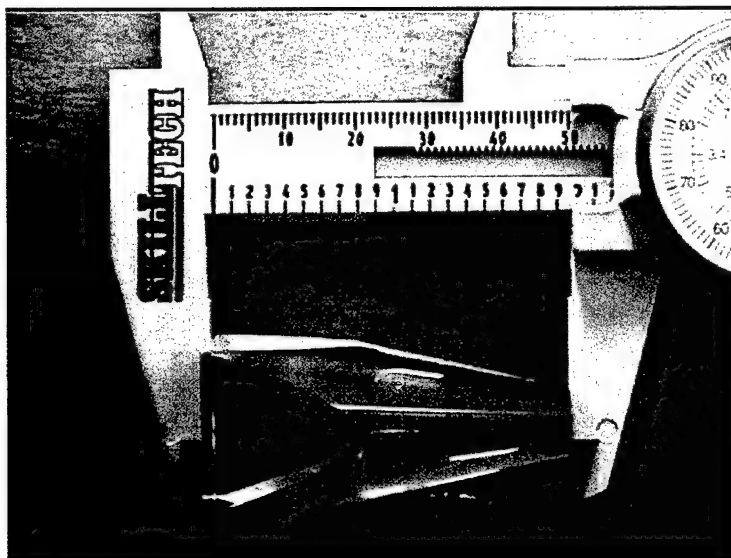
Figure 20: Lucite Light Guide.

attenuation length of lucite was not done, but since the material is generally transparent the study was conducted using two large values for the attenuation length. Assuming an attenuation length of 1.0×10^4 mm, only an average of 6.9% of the photons were transmitted through the guide. With an attenuation length of 1.0×10^8 mm, the average number of photons reaching the end increased to 23%. During this study, it was not determined if the photon escaped the light guide, only if they intersected the end. So due to the geometry and reduced area of the guide, the large majority of the photons were reflected back to the square end of the guide or were absorbed in the guide. Garwin [13] addresses the transmission of radiation through a light pipe and determines that in an adiabatic guide the radiation conducted from an area A to a smaller area A_1 is just A_1/A of the radiation entering through surface A. If our light guide were adiabatic, which it

is not, then 14.6% of the radiation would be expected to be conducted through the guide. In any case it would have been better not to use a light guide since it would have been too bulky for KAMI, creating too much dead space.

Using the various combinations of coating, surface condition, and configuration, the Monte Carlo was run to determine the number of photons that entered the glass of the PMT for each charged particle. Once the number of photons entering the glass have been determined, the properties of the PMT were used in order to determine the number of photo-electrons produced (see section 3.3).

3.3 Photo-Electrons Produced in PMT, Gain of PMT, and Single Photon Response

Once the number of photons at each wavelength that have entered into the glass window of the PMT was known, the cathode sensitivity data from figure 10 was used to determine the quantum efficiency for each photon. The quantum efficiency (equation 32) of the PMT is the percentage of incident photons that produce a photo-electron.

$$Q.E. = \frac{S_k hc}{e\lambda} * (100\%) \tag{32}$$

In equation (32), S_K is the cathode sensitivity measured in mA/W, h is Planck's constant, c is the speed of light, e is the charge of the electron, and λ is the wavelength of the photon in nanometers. The graphical data for the cathode sensitivity is summarized in table 5. Once the number of photo-electrons is known for a charged particle traveling through the cube, the result from many

Wavelength Range (nm)	Cathode Sensitivity (mA/W)	Quantum Efficiency (%)
400–413	62	19.2–18.6
414–428	63	18.6–18.2
429–442	61	17.6–17.1
443–456	60	16.8–16.3
457–471	57	15.5–15.0
472–485	54	14.2–13.8
486–499	50	12.7–12.4
500–513	45	11.2–10.9
514–528	34	8.2–8.0
529–542	23	5.4–5.3
543–556	16	3.7–3.6
557–571	12	2.7–2.6
572–585	8.3	1.8–1.8
586–599	5.6	1.2–1.2
600–613	3.0	.6–.6
614–628	1.3	.3–.3
629–642	0.45	.1–.1
643–657	0.1	.02–.02

Table 5: Cathode Sensitivity.

particles[6] is averaged to obtain the average number of photo–electrons for a given setup.

The gain of the PMT must be understood in order to relate the number of photo–electrons produced by the cathode and the distribution recorded by the ADC. The gain could be taken from the data provided by the manufacturer as given in figure 10, or the gain could also determined independently. But both of these methods assume that the incident photon, after passing the quantum efficiency probability, always produces a single photo–electron in the cathode. It does not account for the possibility of anything else happening, such as the photo–electron being produced on the dynode. In order to better relate the number of photo–electrons to the total distribution, the single photon response must be

---

[6]The particles have the energy distribution as described in detail in section 3.1.

studied.

The method used was to examine the spectrum for a single photon produced by pulsing an LED and measuring it with the PMT. The voltage supplied to the LED was set very low so only approximately 10% of the generated pulses actually fired within the gate for the ADC. In this manner a large pedestal was recorded with a peak for the single photon. The spectrum of the single photon was isolated and evaluated in two ways. First the total histogram with the pedestal included was fit to the sum of two functions, a Gaussian for the pedestal and a function
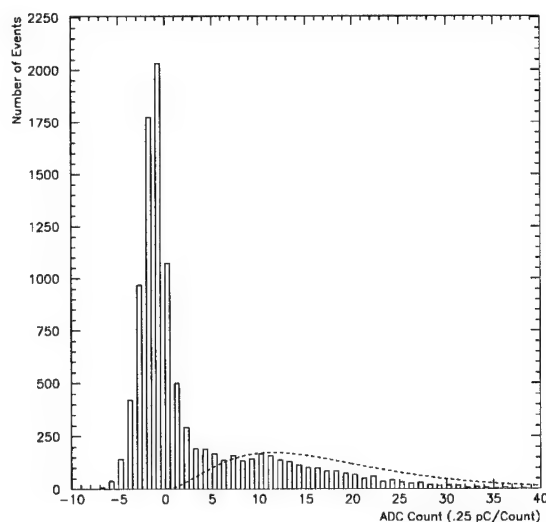

Figure 21: Histogram displaying the single photon spectrum with a large pedestal and functional fit used in the Monte Carlo.

of the following form for the single photon distribution: $p_1 x^2 e^{-p_2 x}$. Fitting the functions to the histogram determine the values for p_1 and p_2. Examining the initial functional fit, the maximum of the function for the single photon spectrum is pulled lower than the maximum in the histogram by noise associated with the pedestal. Additionally there is a zero offset for the pedestal. The actual function

used in the Monte Carlo to transfer from single photons to the total charge distribution was shifted in order to account for the offset. The function used in the Monte Carlo simulation is plotted on top of the single photon spectrum in figure 21.

The second method fit the pedestal to a Gaussian and then subtracted that histogram from the combined one, leaving only the single photon distribution as a histogram. Using the histogram to weigh the photo–electrons produced nearly the exact same results as the first functional fit. The resulting function or histogram was then used to weight each photo–electron as it was produced in the PMT. In this manner the total charge produced in the ADC was simulated for each charged particle.

Name	Description
	PMT Transverse to Particle Direction
CONFIG1	$NaBi(WO_4)_2$ – PMT
CONFIG2	$NaBi(WO_4)_2$ – Cir Opt Pad – PMT
CONFIG3	$NaBi(WO_4)_2$ – Sq Opt Pad – Light Guide – Cir Opt Pad – PMT
CONFIG4	$NaBi(WO_4)_2$ – Opt Grease – Light Guide – Cir Opt Pad – PMT
	PMT Parallel to Particle Direction
CONFIG5	$NaBi(WO_4)_2$ – Cir Opt Pad – PMT (Below)
CONFIG6	$NaBi(WO_4)_2$ – Cir Opt Pad – PMT (Above)

Table 6: Various setup configurations used when taking data with $NaBi(WO_4)_2$.

4 Data Analysis

As stated in section 3, the Monte Carlo simulation was conducted for each configuration shown in figure 11. For convenience the configurations are listed again here in table 6. At the end of the Monte Carlo simulation for a particular setup, 10000 events were generated for each simulation, a variety of distributions are produced. They range from a distribution of the zenith angle for the tracks to total charge distribution produced by the PMT. Of course the charge distribution is the most important, since that is the distribution which is compared to the data to determine how well the simulation is representing the actual behavior of the system. The Monte Carlo and data comparison will be presented in several ways. First some general information about the Monte Carlo distribution will be covered. Secondly the histograms for the charge distribution for the primary configurations will be directly compared. Lastly the remaining configurations will be listed in graphical and tabular format noting the peak and mean values for both the Monte Carlo and the data.

4.1 Monte Carlo Distributions

The various distributions of interest for the Monte Carlo are summarized for CONFIG2 in figure 22. Each distribution provides insight into the whether the simulation is working as expected and that the assumptions that were made were input correctly into the Monte Carlo. Most of the distributions in figure 22 are
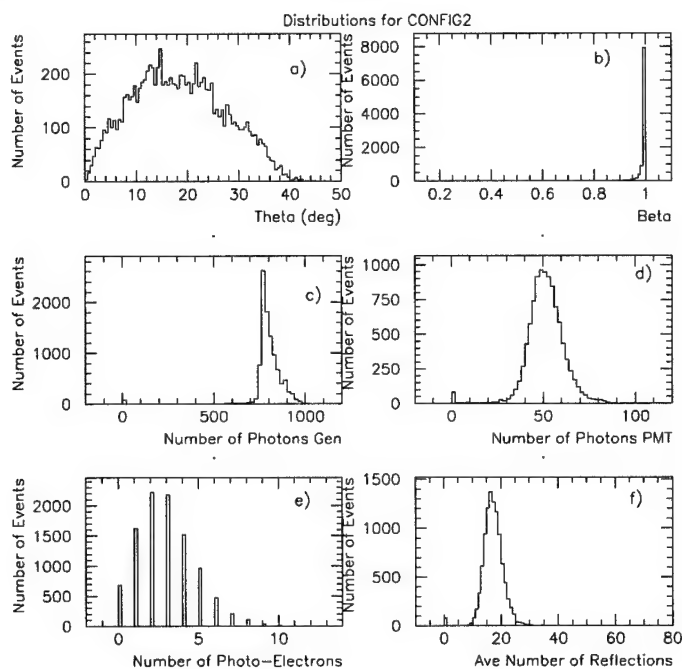

Figure 22: Various distributions produced by the Monte Carlo for the CONFIG2 setup. a) θ, b) β, c) Number of photons generated per particle, d) Number of photons that entered the PMT per particle, e) Number of photo-electrons produced after quantum efficiency applied, f) Average number of reflections per particle entering PMT.

self–explanatory, but note that the average number of reflections (f) is only for those particles entering the PMT. Other particles may have more or less before they are absorbed. Periodically a photon may reflect more than 200 times prior to being absorbed. All of the distributions are as expected and indicate that the Monte Carlo is working properly based on the inputs given.

Photon Statisics (CONFIG2)				
Total Number of Photons Generated: 860				
# Hits on Rect Surface w/ PMT	# Hits Disc Without Foil	# Hits Glass of PMT	# Photons Enter PMT	# Pho–Elec Produced
2019	284	44	44	5

Table 7: Photon statistics inside $NaBi(WO_4)_2$ detector and at its interfaces for a single charged particle track. # Hits on Rect Surface w/ PMT: The number of times the square surface connected with the PMT was hit by all of the photons produced by this example charged particle. # Hits Disc Without Foil: The number of times the surface of the detector the size of the PMT, where no foil is present was hit by all photons. # Hits Glass of PMT: The number of photons to hit the glass of the PMT (occurs once per photon). The last two columns are self-evident.

Besides the distributions, information on the behavior of the photons at the interfaces also indicates whether the simulation is functioning properly. Presented in table 7 are statistics on the actions of photons, generated by a single charged particle, inside the $NaBi(WO_4)_2$ detector and its interfaces. Again this information provides insight as to whether the Monte Carlo is working properly. As the different configurations with different indices of refraction are used, a corresponding change should be seen in the statistics at the interfaces, which is the case.

4.2 Monte Carlo vs Observed Data

Although many of the items addressed in section 4.1 will determine if the mechanics of the Monte Carlo simulation are working properly, the Monte Carlo must be compared with the observed data to determine if the simulation is truly modeling the system. For this thesis all of the observed data was in the form of a total charge distribution. The first comparison shown is for CONFIG2 (PMT trans-

verse to direction of particle), see figure 23. As can be seen in the histograms,
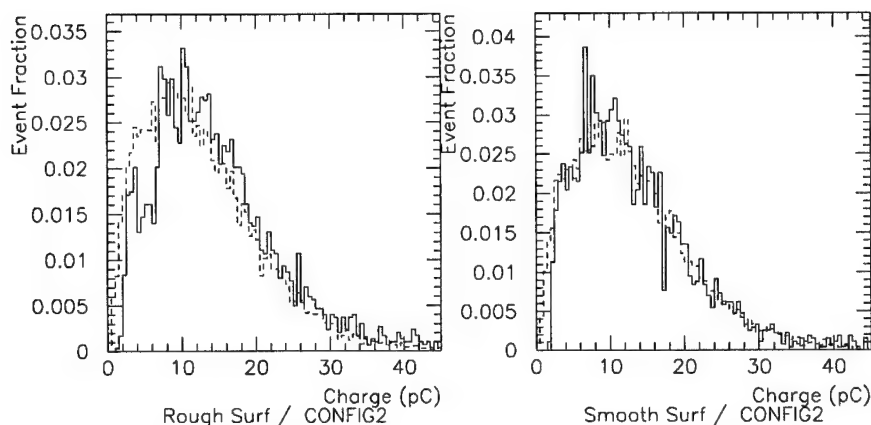

Figure 23: Monte Carlo (dashed) and data (solid) comparison of the charge distribution. This figure shows the results for CONFIG2 for both the rough surface (left) and smooth surface (right).

there is good agreement between data (solid lines) and Monte Carlo (dashed lines) for the smooth surface, yet not as good agreement for the rough surface. Note that these Monte Carlo distributions have the single photon response adjustment described in section 3.3. The discrepancy for the rough surface is most likely contributed to the modeling of the rough surface. Although the procedure was sound and the results showed good agreement no attempt was made to investigate the range of σ leading to an acceptable agreement.

Next configuration used in the comparison is CONFIG5 (PMT inline with the direction of the particle). Shown in figure 24 are the histograms for the data (solid lines) and two Monte Carlo (dashed and dotted lines) simulations. The lower Monte Carlo (dashed lines) was constructed by positioning the trigger counters perfectly above one another with 63 mm of separation due to the apparatus
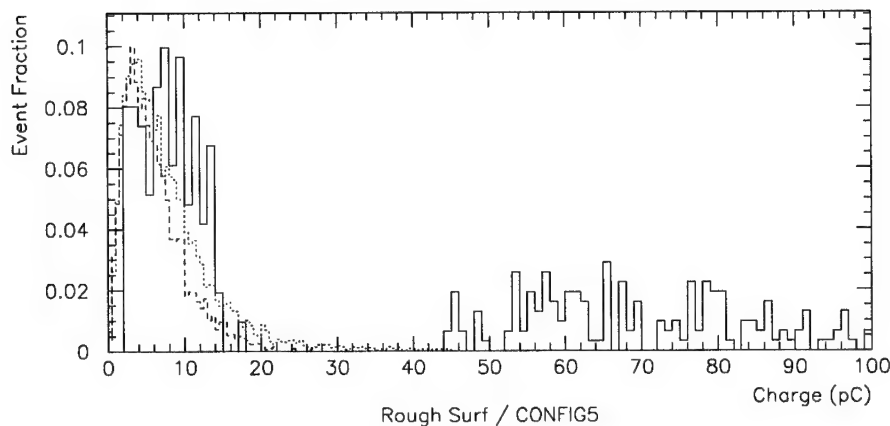
Figure 24: Histograms showing Monte Carlo (dashed and dotted) and data (solid) comparison of the charge distribution. Monte Carlo 1 (dashed) allowed zenith angles 0°–18°, Monte Carlo 2 (dotted) allowed zenith angles 0°–35°. This figure shows the results for CONFIG5 with the rough surface. The contributions of the PMT and optical pad alone (no cube data set) has already been subtracted.

supporting the PMT and the PMT itself. With this geometry the zenith angle could only range from 0° to near 18° while still satisfying the trigger. The second Monte Carlo (dotted lines) was constructed by positioning the trigger counters with an offset of about 10 mm compared with the geometry above. The offset was put in to determine the affects that it would have on the charge distribution and because an offset could have been possible with this configuration since the trigger counters are 63 mm apart. The offset geometry allows the zenith angle to range up to 35°.

This configuration possess other difficulties when comparing Monte Carlo and data since the observed data has two distinct peaks. The combined spectrum is perhaps due to Cherenkov radiation occurring inside the glass of the PMT now that the PMT is facing in the particle direction. This process was not modeled

in the Monte Carlo simulation. So in order to compare the data and the Monte Carlo, the spectrum recorded with no cube in place (just the optical pad and the PMT) was subtracted from the combined data prior to comparing it with the Monte Carlo. This causes the abrupt cut on the data, rather than the usual long tail. The peak at much higher charge is due to some combination of the detector and the PMT, but it is not considered when comparing the data and the Monte Carlo, only the first peak is compared. Even with these extra considerations, there is poor agreement for the first peak. In another attempt to determine the cause of the discrepancy, the particle β was fixed at .7 (momentum of 0.1 GeV/c for μ) and θ was allowed to vary as in the other simulations. The resulting spectrum is plotted with the data in figure 25. This distribution
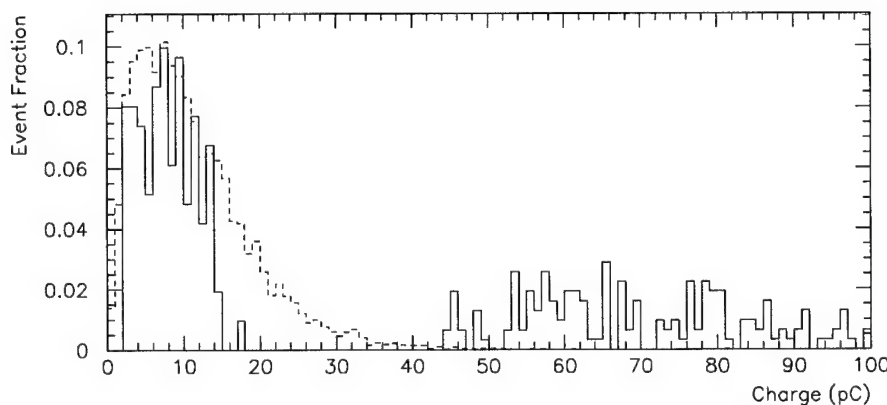

Figure 25: Monte Carlo (dashed) and data (solid) comparison of the charge distribution. This figure shows the results for CONFIG5 with the rough surface. The Monte Carlo has a particle distribution with $\beta = 0.7$, yet θ may still vary.

implies that although less photons are produced with the lower β, more of the photons are likely to leave the detector since the Cherenkov angle will be smaller.

While this forced change in the spectrum of the cosmic rays improves the Monte Carlo fit to the data in CONFIG5, it degrades the agreement between data and Monte Carlo when applied to the transverse configurations (CONFIG2). This also brings into question how well the cosmic ray spectrum is known, especially for zenith angles less than 18° and energies below 0.2 GeV/c. As stated before in section 3.1, most experiments on cosmic rays have not measured the muon flux below energies of 0.2 GeV/c. As another test the momentum spectrum for the incident particles was adjusted. The spectrum was fixed at a constant value for all energies below 0.2 GeV/c for each separate curve corresponding to a different value of θ. After running the simulation with the new momentum distribution, the transverse configuration (CONFIG2) was degraded again and the spectrum for the inline setup (CONFIG5) was only very slightly improved.

The remainder of the Monte Carlo and data charge distribution comparisons are presented as histograms and summarized in table 8 where the peak and mean for each configuration setup are annotated. The trends addressed above are evident throughout the table. The simulation of the smooth surface (paint or foil) is in excellent agreement with the data. On the other hand, the comparison for the rough surface shows that the modeling of that surface in not completely accurate. In the data the rough surface typically increased the amount of light exiting the detector, but the Monte Carlo does not match this observation. Additionally, the transverse configurations are better modeled than the in–line configurations. Again this could be contributed to the lack of knowledge of the muon momentum spectrum for energies less than 0.2 GeV/c.

Charge Distribution (pC)					
Configuration	Data		Monte Carlo		Figure
	Peak	Mean	Peak	Mean	Number
Paint Coating					
Sm–CONFIG2	8.3	13.19	8.49	12.91	27
Foil Coating					
Sm–CONFIG2	9.5	13.24	9.5	12.78	23
R–CONFIG1	5.25	8.3	4.0	7.63	26
R–CONFIG2	11.77	14.52	8.35	12.64	23
R–CONFIG3	4.49	8.26	3.95	10.88	29
R–CONFIG4	5.22	9.3	3.78	10.83	29
R–CONFIG5	7.67	11.0	4.3	7.78	24
R–CONFIG6	5.96	14.62	3.55	6.58	28

Table 8: Summary of charge distribution peaks and means. Sm - smooth surface, R - rough surface.
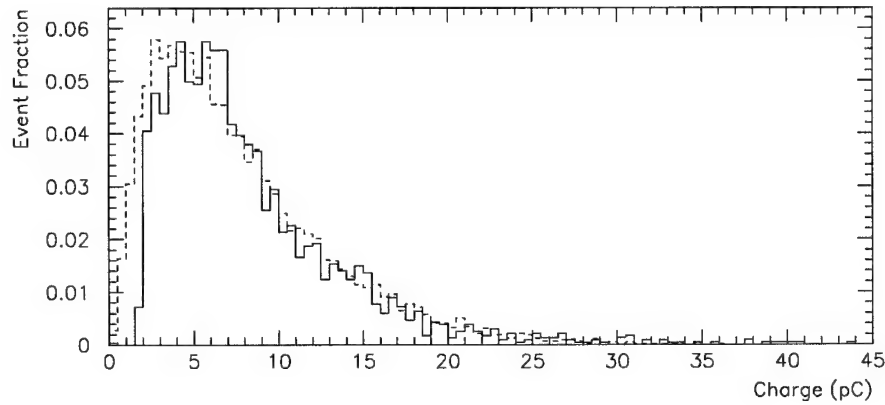

Figure 26: Monte Carlo (dashed) and data (solid) comparison of the charge distribution. This figure shows the results for CONFIG1 with the rough surface.
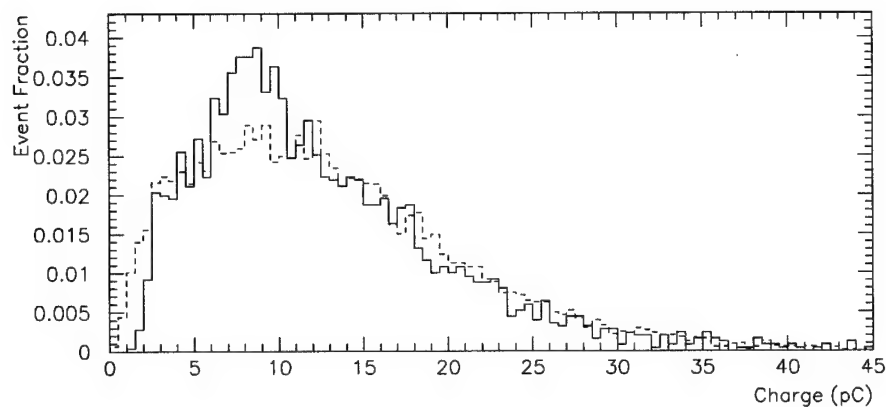
Figure 27: Monte Carlo (dashed) and data (solid) comparison of the charge distribution. This figure shows the results for CONFIG2 with the smooth surface and paint coating.
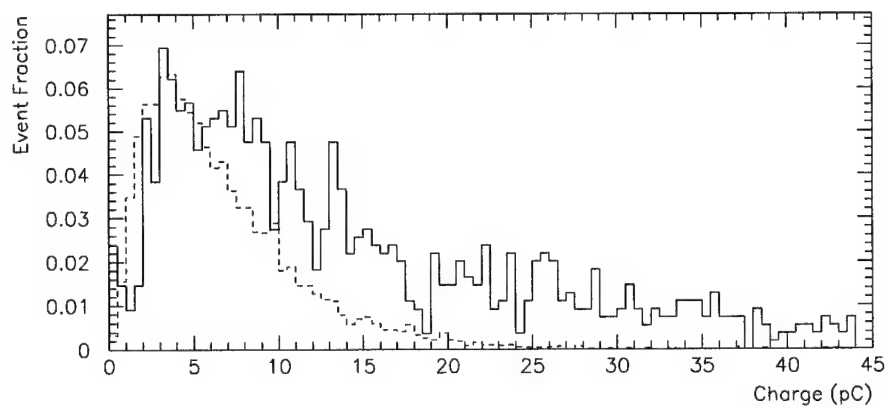

Figure 28: Monte Carlo (dashed) and data (solid) comparison of the charge distribution. This figure shows the results for CONFIG6 with the rough surface.
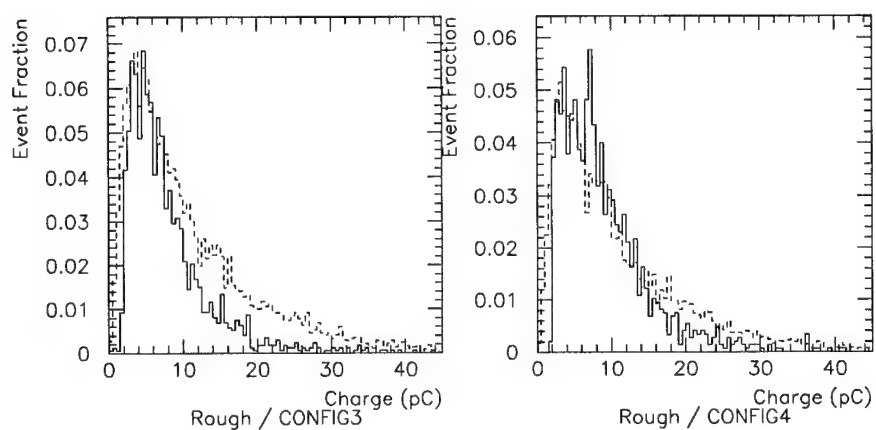
Figure 29: Monte Carlo (dashed) and data (solid) comparison of the charge distribution. This figure shows the results for CONFIG3 (left) and CONFIG4 (right) with rough surfaces. The Monte Carlo distribution is higher do to only estimating the attenuation length for lucite and treating it as wavelength independent.

5 Conclusion

After studying $NaBi(WO_4)_2$ and Cherenkov radiation over the past year, I conclude that it does make a good Cherenkov radiator and could be useful in future experiments.

While it does make a good Cherenkov radiator, there are still challenges in getting the maximum number of photons out of the material in order to identify particles. I determined that the best configuration involved roughing the surface of the detector on the side where the PMT is located, using the optical interface pads, and positioning the PMT facing transversely to the direction of the charged particle (CONFIG2). The problem then becomes CONFIG2 is not the optimal configuration which will be used in particle physics experiments, CONFIG5 will be the desired configuration. CONFIG5 may still be very productive for particle experiments since there are two fundamental differences in my study of $NaBi(WO_4)_2$ and how it will most likely be used in experiments. First I studied the effects of a single charged particle going through the material, but the experiments will be more likely be dealing with showers of charged particles produced from an interaction in the $NaBi(WO_4)_2$ detector. For example, the experiment may be trying to identify neutral particles such as neutrons. The second difference is since experiments have showers of charged particles, they will also have a far greater number of Cherenkov photons produced thus increasing the signal measured by the PMT. Also the size of the detector sections will be larger for the particle experiments.

Further research should be conducted using $NaBi(WO_4)_2$ in an environment where the beam characteristics are well known and thus can be simulated with

high confidence. In such an environment, a more detailed study of the various configurations could be conducted.

References

[1] T. Alexopoulos *et al.* *A Proposal for a Precision Measurement of the Decay $K_L \rightarrow \pi^0 \nu \bar{\nu}$ and Other Rare Processes at Fermilab Using The Main Injector − KAMI.*

[2] G.I. Britvich *et al.* Radiation resistant multicomponent inorganic materials for homogeneous e.m. calrimeters. *Nucl. Instr. & Meth.*, A(321):64–68, 1992.

[3] T. Inagaki *et al.* Measurement of the $K_L \rightarrow \pi^0 \nu \bar{\nu}$ decay, KEK Propsal, June 1996.

[4] John David Jackson. *Classical Electrodynamics.* John Wiley & Sons, Inc., third edition, 1999. Pages: 633-637.

[5] J. V. Jelley. *Čerenkov Radiation and its applications.* Pergamon Press, 1958. Pages: 5-6.

[6] D.E. Groom *et al.* Review of particle physics. *The European Physical Journal C*, 15(1–4):151–152,163, 2000.

[7] J. Kremer *et al.* Measurements of ground–level muons at two geomagnetic locations. *Physical Review Letters*, 83(21):4241–4244, 1999.

[8] B.N. Kalinin *et al.* The investigation of a model of an em calorimeter on $NaBi(WO_4)_2$ crystals. *Nucl. Instr. & Meth.*, A(361):157–160, 1995.

[9] David J. Griffiths. *Introduction to Electrodynamics.* Prentice Hall, second edition, 1989. Pages: 360–363.

[10] *Hamamatsu Metal Package Photomultiplier Tube R7400U SERIES.* Data Sheets available online http://www.hamamatsu.com.

[11] Vadim A. Naumov. Atmospheric muons and neutrinos. In *Proceedings of 2nd Workshop on Methodical Aspects of Undereater/Underice Neutrino Telescopes*, 2001. Available at arXiv.org with reference number hep-ph/0201310v1 31 Jan 2002.

[12] Thomas C. Hayes and Paul Horowitz. *Student Manual For The Art of Electronics.* Cambridge University Press, 1989.

[13] R. L. Garwin. The design of liquid scintillation cells. *Review of Scientific Instruments*, 23(12):755–757, 1952.